

Applications of a New 206.5-nm Continuous-Wave Laser Source: UV Raman Determination of Protein Secondary Structure and CVD Diamond Material Properties

JANET S. W. HOLTZ, RICHARD W. BORMETT, ZHENHUAN CHI, NAMJUN CHO,* X. G. CHEN,† VASIL PAJCINI, SANFORD A. ASHER,‡ LUIS SPINELLI, PHILIP OWEN, and MARCO ARRIGONI

Department of Chemistry, University of Pittsburgh, Pittsburgh, Pennsylvania 15260 (J.S.W.H., R.W.B., Z.C., N.C., X.G.C., V.P., S.A.A.); and Coherent Laser Group, Division of Coherent Inc., 5100 Patrick Henry Drive, Santa Clara, California 95056 (L.S., P.O., M.A.)

We demonstrate the utility of a new 206.5-nm continuous-wave UV laser excitation source for spectroscopic studies of proteins and CVD diamond. Excitation at 206.5 nm is obtained by intracavity frequency doubling the 413-nm line of a krypton-ion laser. We use this excitation to excite resonance Raman spectra within the $\pi \rightarrow \pi^*$ amide transition of the protein peptide backbone. The 206.5-nm excitation resonance enhances the protein amide vibrational modes. We use these high signal-to-noise spectral data to determine protein secondary structure. We also demonstrate the utility of this source to excite CVD and gem-quality diamond within its electronic bandgap. The diamond Raman spectra have very high signal-to-noise ratios and show no interfering broad-band luminescence. Excitation within the diamond bandgap also gives rise to narrow photoluminescence peaks from diamond defects. These features have previously been observed only by cathodoluminescence measurements. This new continuous-wave UV source is superior to the previous pulsed sources, because it avoids nonlinear optical phenomena and thermal sample damage; Photoluminescence.

Index Headings: Raman spectroscopy; Instrumentation; Lasers; UV resonance Raman spectroscopy; Protein secondary structure studies; CVD diamond; Photoluminescence.

INTRODUCTION

Advances in spectroscopy often result from advances in instrumentation. In the work reported here, we describe a new UV laser source which emits ~ 4 mW of continuous-wave light at 206.5 and ~ 8 mW at 234 nm. This continuous-wave 206.5-nm source is useful for resonance Raman excitation of numerous molecular species with absorption bands in the 190–220-nm spectral region.¹ It is also useful for nonresonance Raman excitation for species which have only far-UV absorption bands.^{2,3} Excitation in the UV, even out of resonance, generally results in larger Raman cross sections because of the frequency-to-the-fourth-power dependence of light scattering,^{4–6} and because this excitation approaches the absorption bands of all species. In addition, preresonance Raman enhancement dramatically increases the Raman cross sections. Another advantage of UV excitation is that in the condensed-phase fluorescence interference is absent for excitation below 260 nm, because the excited states decay through nonradiative channels.⁷

UV resonance Raman spectroscopy (UVRR) has rapidly advanced over the last decade,^{8,9} and numerous applications have been demonstrated for proteins,^{10–16} nucleic acids,^{17–20} and polycyclic aromatic hydrocarbons.^{21–25} A major difficulty with the previous UV Raman instrumentation is that the laser sources were low-duty-cycle pulsed sources, which could give rise to nonlinear optical phenomena.^{25–29} This consideration was the major motivation of our previous work to develop a continuous-wave excitation source by intracavity frequency doubling an Ar⁺ ion laser.²⁹ This successful effort resulted in convenient UV continuous-wave excitation wavelengths in the 229–257-nm spectral region. In the work reported here, we extend this approach to the 413-nm Kr⁺ ion laser emission line, which, when frequency doubled, gives excitation at 206.5 nm. As demonstrated below, this excitation wavelength can be used directly to excite within the amide $\pi \rightarrow \pi^*$ transitions of peptides and proteins.^{3,30–35} The resulting high signal-to-noise ratio spectra are dominated by the protein amide vibrations, which can be analyzed to determine protein secondary structure. In addition, we demonstrate the utility of this 206.5-nm excitation to study diamond structure.³⁶ Excitation within the diamond bandgap results in high signal-to-noise ratio diamond phonon Raman spectra and leads to photoluminescence emission from intrinsic and extrinsic diamond defect structures. The strong diamond absorption bandgap results in less than 1- μm penetration of the

UV resonance Raman spectroscopy (UVRR) has rapidly advanced over the last decade,^{8,9} and numerous applications have been demonstrated for proteins,^{10–16} nucleic acids,^{17–20} and polycyclic aromatic hydrocarbons.^{21–25} A major difficulty with the previous UV Raman instrumentation is that the laser sources were low-duty-cycle pulsed sources, which could give rise to nonlinear optical phenomena.^{25–29} This consideration was the major motivation of our previous work to develop a continuous-wave excitation source by intracavity frequency doubling an Ar⁺ ion laser.²⁹ This successful effort resulted in convenient UV continuous-wave excitation wavelengths in the 229–257-nm spectral region. In the work reported here, we extend this approach to the 413-nm Kr⁺ ion laser emission line, which, when frequency doubled, gives excitation at 206.5 nm. As demonstrated below, this excitation wavelength can be used directly to excite within the amide $\pi \rightarrow \pi^*$ transitions of peptides and proteins.^{3,30–35} The resulting high signal-to-noise ratio spectra are dominated by the protein amide vibrations, which can be analyzed to determine protein secondary structure. In addition, we demonstrate the utility of this 206.5-nm excitation to study diamond structure.³⁶ Excitation within the diamond bandgap results in high signal-to-noise ratio diamond phonon Raman spectra and leads to photoluminescence emission from intrinsic and extrinsic diamond defect structures. The strong diamond absorption bandgap results in less than 1- μm penetration of the

Received 9 February 1996; accepted 3 July 1996.

* Present address: Department of Chemistry, University of California—Los Angeles, Los Angeles, CA 90024.

† Present address: Section on Metabolic Analysis and Mass Spectrometry, NICHD, National Institute of Health, 10 Center Drive, MSC1580, Room 6C208, Bethesda, MD 20892.

‡ Author to whom correspondence should be sent.

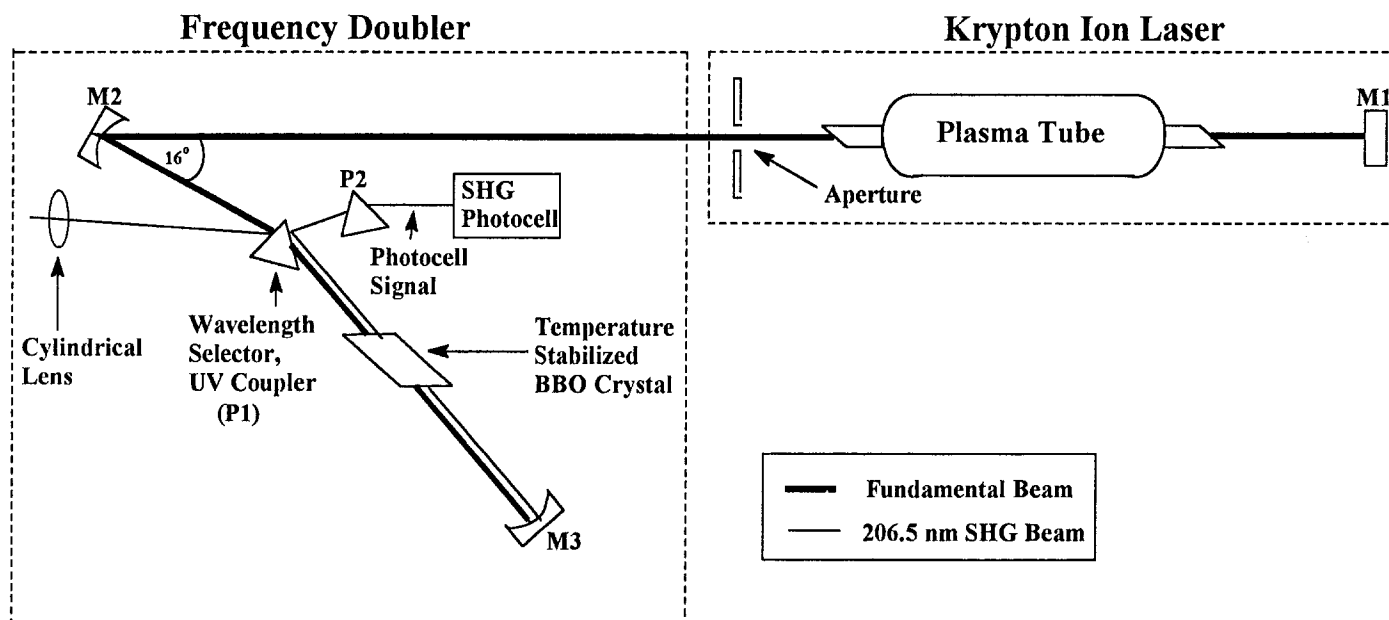


FIG. 1. Schematic diagram showing the optical layout of the Coherent Innova 400 intracavity frequency-doubled krypton-ion laser.

206.5-nm light; thus the spectra probe near-surface species.

EXPERIMENTAL

Materials. Concanavalin A (con A), trypsin, ribonuclease A (RNase A), cytochrome *c* (cyt *c*), bovine serum albumin (BSA), hemoglobin (Hb), and myoglobin (Mb) were purchased from Sigma Chemical Co. Each protein was dissolved in pH 7 phosphate buffer. Sodium perchlorate was used as the internal standard. Angiotensin II (AII) was purchased from Sigma Chemical Co. Dodecylphosphocholine (DPC) was obtained from Avanti Polar Lipids, Inc.

Instrumentation. Figure 1 shows an optical schematic diagram of the intracavity frequency-doubled continuous-wave krypton-ion laser, while Table I lists its output wavelengths and powers. The krypton-ion laser fundamental lines occur above 337.5 nm, and the powers listed are those typically available from this large-frame Coherent Innova 400 krypton-ion laser. The listed output

powers of the frequency-doubled 206.5- and 234-nm lines were measured in our laboratory.

The intracavity doubling optics are placed at the normal output port of the laser; the front mirror output coupler is removed, and the laser cavity is extended to include the frequency-doubling optics. The curved, folding mirror **M2** directs the fundamental beam towards the Brewster-angle wavelength selection prism, **P1**. **P1** both selects lasing for the fundamental Kr^{++} line at 413 nm and separates the second-harmonic-generated (SHG) beam at 206.5 nm from the fundamental intracavity beam. The fundamental beam is focused by **M2** into a β -barium borate (BBO) doubling crystal. Since this is a standing-wave cavity, two counterpropagating second harmonic beams are generated. The 206.5-nm beam directed toward **M3**, which is a total reflector at 413 nm, is partly absorbed and partly reflected. The other 206.5-nm beam, traveling in the opposite direction, is refracted by **P1** into the collimating cylindrical lens, which focuses the beam outside the doubler. **P1** has a very low reflectivity for the *p*-polarized fundamental intracavity beam. However, the *s*-polarized SHG beam is partly reflected ($\sim 20\%$) at both **P1** surfaces. The reflection off the first surface of **P1** is directed to a photocell through a second prism, **P2**, which eliminates any residual 413-nm light. The photocell detector is the sensor for a control system, which regulates the output power of the SHG beam by adjusting the plasma tube current to stabilize the laser SHG output power. The temperature of the BBO crystal is maintained at $\sim 55^\circ\text{C}$. The laser cavity is constantly purged with N_2 .

A complex SHG beam (206.5 nm) profile is observed immediately outside the laser cavity. Figure 2 shows laser beam contour intensity plots as recorded by a laser beam analyzer (Beam Master, Coherent) for 0.5-, 2.0-, and 3.0-mW output powers. The changes in the intensity profile with increasing SHG power indicate the presence of a strong thermal lensing. This effect is likely due to the absorption of the fundamental as well as the SHG radi-

TABLE I. Krypton-ion laser wavelengths and output powers.

| Wavelength (nm) | Power (mW) |
|-----------------|------------|
| 206.5 | 4 |
| 234 | 8 |
| 337.5–356.4 | 2000 |
| 406.7 | 900 |
| 413.1 | 1800 |
| 415.4 | 280 |
| 468.0 | 500 |
| 476.2 | 400 |
| 482.5 | 400 |
| 520.8 | 700 |
| 530.9 | 1500 |
| 568.2 | 1100 |
| 647.1 | 3500 |
| 676.4 | 900 |
| 720.8 | 45 |
| 752.5 | 1200 |
| 793.1–799.3 | 300 |

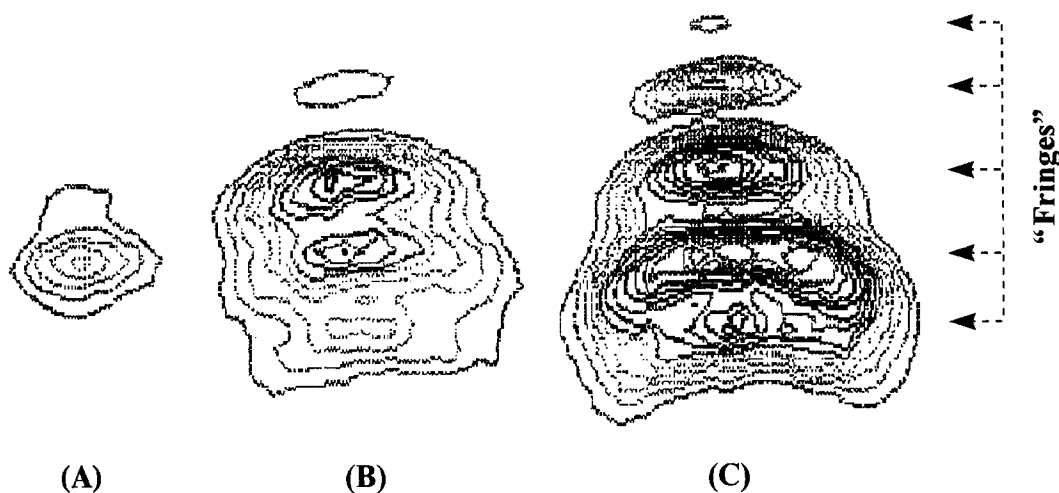


FIG. 2. Contour plots of the 206.5-nm beam intensity profile taken for three different laser powers: (A) 0.5 mW, (B) 2.0 mW, and (C) 3.0 mW.

ation, which is very close to the absorption edge of BBO (~ 200 nm). The BBO crystal optical absorption and the resulting optical damage limit the maximum 206.5-nm output power available. We have observed a maximum output power of ~ 5 mW at a plasma tube current of 55 A, but find that 206.5-nm output powers greater than 4.5 mW quickly damage the BBO crystal. In contrast, operating powers of 3–4 mW give a BBO crystal life span in excess of 400 h. We typically utilize a 206.5-nm beam output power of 3 mW, and focus the beam to spot sizes of ~ 100 μm at the sample.

The Raman scattered light is collected by using a 135° back-scattering geometry and is dispersed by a Spex Triplemate spectrometer.^{8,9} The spectra were detected with either an Intensified Reticon photodiode array (EG&G PAR Model 1420) or an intensified charge-coupled device (CCD) detector (Princeton Instruments, Inc. Model ICCD-1024 MS-E).

RESULTS AND DISCUSSION

This laser is the best presently available excitation source for linear spectroscopy in the 200-nm spectral region. Other competing sources either are not narrow wavelength sources or are low-duty-cycle pulsed sources which give rise to nonlinear optical phenomena.^{25,29} This continuous-wave 206.5-nm source is of general utility for resonance Raman excitation for the numerous species with absorption bands in the 190–220-nm spectral region.¹

In the work here, we demonstrate applications of this 206.5-nm continuous-wave Raman excitation for biophysical and bioanalytical applications to study protein secondary structure; the 206.5-nm excitation occurs directly into the protein backbone amide $\pi \rightarrow \pi^*$ transitions, which results in the selective enhancement of amide vibrations.^{6,30,31,37} We also demonstrate a materials science application where we simultaneously excite, for the first time, the Raman and photoluminescence spectrum of diamond deep within its bandgap.

Protein Secondary Structure Studies. Figure 3 shows the continuous-wave 206.5-nm excited UVRR spectra of con A, trypsin, RNase A, cyt *c*, BSA, Hb, and Mb. These proteins show quite different secondary struc-

tures, and they especially differ in their α -helical content (Table II); the con A is only $\sim 2\%$ α -helix, while Mb is $\sim 79\%$ α -helix. The 932-cm^{-1} bands in the Raman spectra are due to perchlorate, added as an internal standard, while the other bands derive mainly from amide vibrations of the peptide backbone. The 206.5-nm excitation occurs within the peptide backbone amide $\pi \rightarrow \pi^*$ transitions.³⁷ Thus, selective resonance enhancement occurs for the amide vibrations, and the spectra are dominated by amide bands. The intense bands at $\sim 1655\text{-cm}^{-1}$ derive from the amide I vibrations, which have large contributions from C=O stretching and smaller contributions from C–N–H bending and from other amide motions.³¹ The 1617-cm^{-1} bands mainly result from the aromatic ring breathing vibrations of the aromatic amino acids, Phe, Tyr, and Trp. Tyr and Trp have strong absorptions around the 225-nm spectral region.^{38,39}

The bands at $\sim 1550\text{-cm}^{-1}$ derive mostly from the amide II vibration, which involves C–N stretching and some C–N–H bending.^{40,41} The broad bands between 1200 and 1300-cm^{-1} derive mainly from the amide III vibrations, which have large contributions of C–N stretching and C–N–H bending. The $\sim 1390\text{-cm}^{-1}$ band present in the protein spectra, except for Mb, is predominantly a C_α -H bending mode, which is enhanced because of the smaller components of C–C and C–N stretching.³¹ The intensities of this C_α -H bending band, and the intensities and frequencies of the amide III band, are especially sensitive to secondary structure.^{34,37} The C_α -H bending mode has a vanishingly small intensity for the α -helical structure.³⁴ Thus, this band is not present in the Mb spectrum because this protein is mainly α -helix.

The right column of Fig. 3 shows the resonance Raman spectra of these proteins dissolved in D_2O . Deuterium exchange at the amide N–H bond dramatically changes the normal mode composition of the amide vibrations.³¹ The amide II and III bands disappear, and a much stronger amide II' band occurs at $\sim 1460\text{-cm}^{-1}$. The amide II and III vibrations have significant coupling of C–N stretching and the N–H bending; however, the increased deuterium mass causes this coupling to disappear, and the amide II' vibration has little N–D bending. The amide II' band has a much higher cross section than those of the

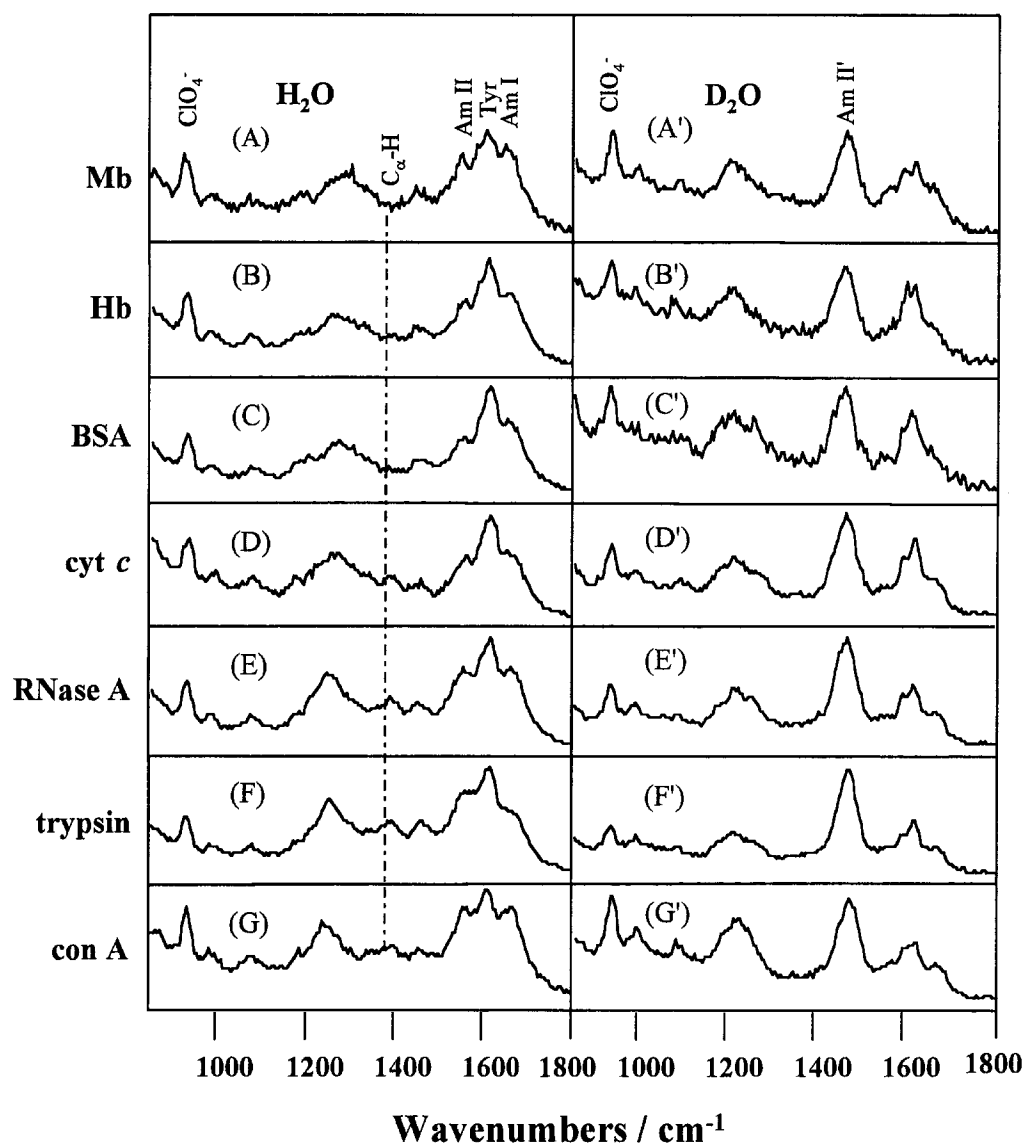


FIG. 3. The 206.5-nm excited Raman spectra of (A) myoglobin (Mb), (B) hemoglobin (Hb), (C) albumin (BSA), (D) cytochrome *c* (cyt *c*), (E) ribonuclease A (RNase A), (F) trypsin, and (G) concanavalin A (con A) dissolved in H₂O and D₂O. Protein concentrations are 0.5 mg/mL, except for concanavalin A, which is 0.25 mg/mL. All proteins were dissolved in pH 7 phosphate buffer containing 0.15 M sodium perchlorate. Laser power was ~3 mW with a spot size ~150 μm. The spectra were collected with a total accumulation time of 33 min. The spectral resolution is ~30 cm⁻¹.

amide II and III bands and is well separated from the Tyr, Phe, and Trp bands. The C_α-H bending mode at ~1400 cm⁻¹ is not evident in the UV Raman spectra for peptide amide groups where the N-H bond is deuterated; deuteration removes the contribution of C-C stretching to this vibration.³¹ Deuteration downshifts the amide I band by ~5 cm⁻¹ (Fig. 3). In contrast, the frequency of the amide II' band is almost independent of secondary structure.^{31,37}

The Raman cross sections of the amide bands depend on the amide π→π* transition absorptivity, which depends upon secondary structure; a strong hypochromism occurs in the α-helix structure, which decreases the Raman cross sections.^{13,37,42} The absorptivity and Raman cross sections of the amide bands are more similar for the β-sheet and random coil structures, although significant frequency alterations occur.³⁷ The Raman intensity of the amide II' band can be used to estimate the protein α-helix content. Figure 4, which plots the intensity ratio

of the amide II' band to the internal standard band vs. the α-helix content, also shows a least-squares fitted line described by Eq. 1:

$$\mathcal{R} = -0.031P + 5.1 \quad (1)$$

where \mathcal{R} is the intensity ratio of the amide II' band to the internal standard band, and P is the percent α-helix. Equation 1 can be rearranged to make it convenient for determining the percent α-helix content from the measured Raman intensity ratio:

$$P = \frac{5.1 - \mathcal{R}}{0.031} \quad (2)$$

Equations 1 and 2 are valid for the 206.5-nm excited 0.5 mg/mL protein samples containing 0.15 M sodium perchlorate. It is likely that this equation can be scaled to other protein and internal standard concentrations:

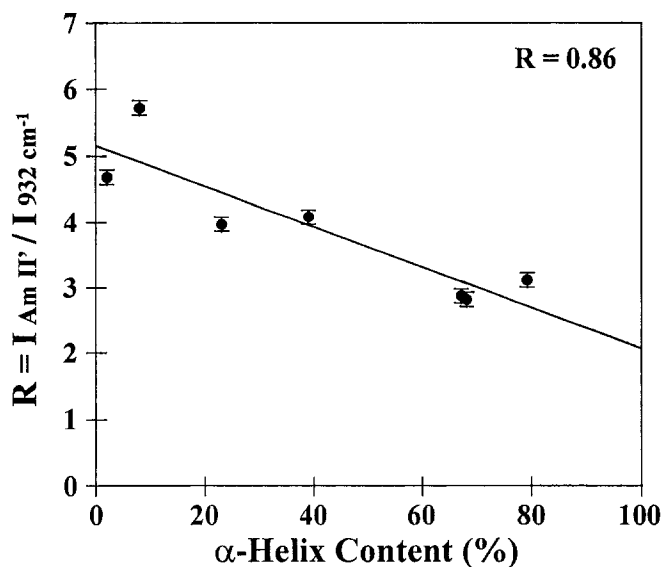


FIG. 4. Dependence of the amide II' to the 932-cm⁻¹ internal standard intensity ratio on the protein percent α -helix content. The correlation coefficient R and experimental error are also shown.

$$\mathcal{R} = 3.33 \frac{C_{\text{int}}}{C_p} \mathcal{R}' \quad (3)$$

where \mathcal{R}' is the intensity ratio of the measured amide II' to perchlorate 932-cm⁻¹ band, and C_{int} is the internal standard concentration (molar), while C_p is the protein concentration (mg/mL). While this equation will be useful for concentrations other than the 0.5-mg/mL protein and the 0.15 M perchlorate used here, some quantitative errors will arise from alterations in the sample self-absorption at other protein concentrations. The intensity ratios \mathcal{R} and \mathcal{R}' can be directly and conveniently measured since the amide II' band occurs in a spectral region well separated from any other protein Raman bands.

The intensity of the C_α-H bending band is also sensitive to the secondary structure, and the C_α-H bending band vanishes for the α -helix structure. Figure 5 plots the C_α-H bending and internal standard band intensity ratio as a function of α -helix content, along with the least-squares fitted line:

$$\mathcal{R}_{\text{CH}} = -0.015P + 1.4 \quad (4)$$

where \mathcal{R}_{CH} is the ratio of the C_α-H bending intensity to the perchlorate intensity for 0.5-mg/mL protein and 0.15 M sodium perchlorate concentration. Equation 4 can be rearranged to directly relate the measured intensity ratio to the α -helix content:

$$P = \frac{1.4 - \mathcal{R}_{\text{CH}}}{0.015} \quad (5)$$

A correlation of C_α-H bending band intensity with the α -helix content was observed previously by Wang et al. with the use of deconvolution.³⁴ It appears that essentially no other protein features underlie the C_α-H bending band when excited at 206.5 nm.

The intensity values used for calculating the intensities of the amide II' band and C_α-H bending are easily obtained from the protein spectrum by merely measuring the peak height from a linear baseline, which spans the

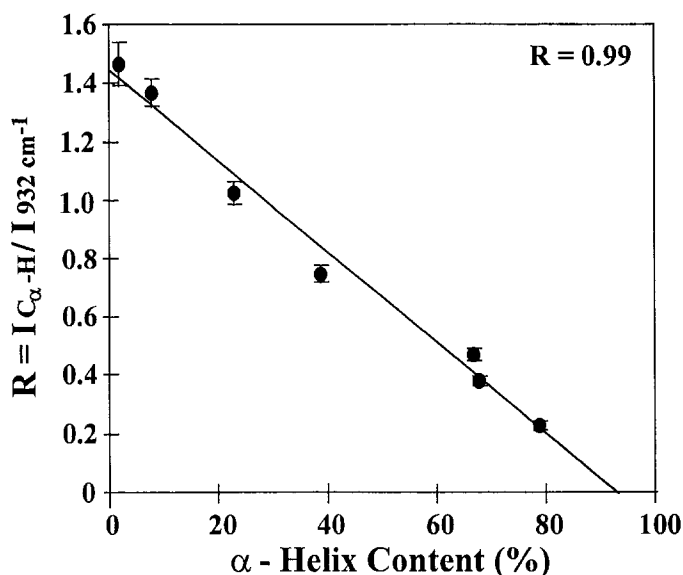


FIG. 5. Dependence of the C_α-H bending band to the 932-cm⁻¹ internal standard band intensity ratio on the protein α -helix content. The correlation coefficient R and experimental error are also shown.

frequency interval between 1100 and 1800 cm⁻¹. A similar approach is used to calculate the internal standard band intensity.

The amide I and II bands are significantly overlapped by the aromatic ring breathing vibrational bands of Tyr, Phe, and Trp. Raman spectra of these aromatic amino acids have been well characterized, and the frequencies show only a weak dependence on environment.^{10,26,28,38,43} Thus, it is possible to numerically subtract out the Tyr, Phe and Trp contributions, to leave spectra that are completely dominated by the amide bands. Figure 6 shows the spectra of con A and Mb, where the contributions of the aromatic amino acids were removed by subtraction of Tyr, Phe, and Trp spectra; the relative amount of each amino acid subtracted was scaled to the content of each aromatic amino acid present in the protein. The arrows at ~1610 cm⁻¹ indicate the region from which the contributions of Phe, Trp, and Tyr were removed. Protein Raman spectra, shown in Fig. 6, are completely dominated by the amide bands.

Our previous studies³⁷ demonstrated that each of the three common peptide secondary structures gives rise to distinct UVRR spectra. Thus, the UV resonance Raman spectrum $O(\nu)$ can be modeled as the sum of the individual secondary structure spectra weighted by their relative abundance:

$$O(\nu) = \sum_i I_i(\nu)F_i + P(\nu) \quad (6)$$

The individual spectra, $I_i(\nu)$, were first modeled as if they derived from component resonance Raman spectra of the α -helix, β -sheet, and random coil conformations of polyglutamic acid (PGA) and poly-L-glycine (PLL).³⁷ We estimated these basic spectra by averaging the PGA and PLL spectra obtained in the different secondary structure forms. Further refinements, which will be discussed in a future publication,⁴⁴ calculate better $I_i(\nu)$ basis spectra. F_i is the fractional contribution of each secondary structure,

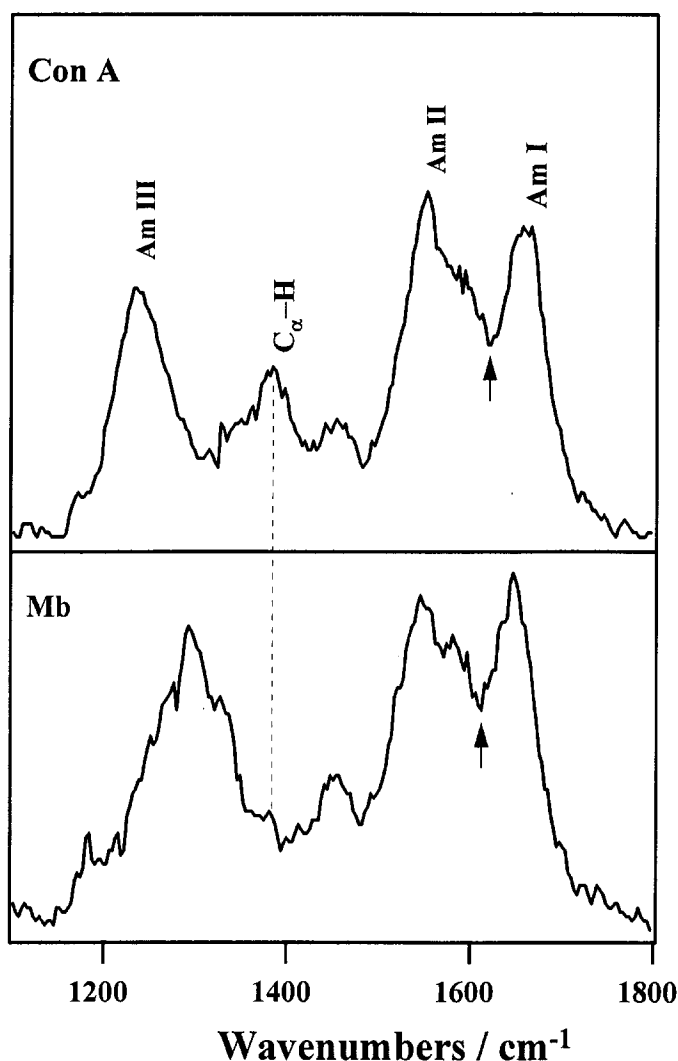


FIG. 6. The H_2O spectra of concanavalin A and myoglobin spectra where the contributions of the aromatic acids (Phe, Tyr, and Trp) were numerically removed from the spectra. The arrows indicate the region from which the contributions from Phe, Tyr, and Trp were subtracted. The magnitude of aromatic amino acid subtracted is proportional to their relative content in each protein.

and $P(\nu)$ is the residual contribution of any nonassigned, nonamide features to the Raman spectrum.

The secondary structural content of a protein can be determined by a best fit of Eq. 6 to the observed protein spectra to determine F_i ; Table II compares the secondary structural content (%) calculated by our model to that obtained by X-ray crystallography⁴⁵⁻⁴⁷ and CD.⁴⁸ Table II shows that, with some interesting exceptions, our results agree relatively well with previous conclusions. Our calculated random coil contribution is consistently lower than literature values that combine the random coil content with protein conformations other than α -helix and β -sheet—for example, the β -turn.

We can also use 206.5-nm excitation to monitor peptide conformation in lipid micelles. Figure 7 shows the 206.5-nm excited Raman spectrum of angiotensin II (AII) in both aqueous and lipid micelle hydrophobic environments. AII (Asp-Arg-Val-Tyr-Ile-His-Pro-Phe) is a linear octapeptide hormone that controls blood pressure and maintains fluid and electrolyte homeostasis.⁴⁹ Figure 7

TABLE II. UV resonance Raman determination of secondary structure of aqueous protein compared to the results obtained from other methods (X-ray and CD).

| | α -Helix content (%) | | β -Sheet (%) | | RC ^a + others (%) | |
|--------------|-----------------------------|-------------------|--------------------|-------------------|------------------------------|-------------------|
| | Raman | Previous | Raman | Previous | Raman | Previous |
| Con A | 5 | 2 ^b | 75 | 60 ^b | 20 | 38 ^b |
| Trypsin | 15 | 8 ^c | 60 | 32 ^c | 25 | 60 ^c |
| RNase A | 30 | 23 ^b | 50 | 40 ^a | 20 | 37 ^b |
| Cyt <i>c</i> | 55 | 39 ^d | 10 | 0 ^d | 35 | 61 ^d |
| BSA | 70 | 68 ^{e,f} | 15 | 18 ^{e,f} | 5 | 14 ^{e,f} |
| Hb | 70 | 67 ^c | 25 | 0 ^c | 5 | 33 ^c |
| Mb | 80 | 79 ^d | 15 | 0 ^d | 5 | 21 ^d |

^a Random coil.

^b See Ref. 46.

^c See Ref. 47.

^d See Ref. 48.

^e See Ref. 49.

^f Data obtained from CD.

shows the spectrum of AII in H_2O , and of AII in micelles of dodecylphosphocholine (DPC), and the difference spectrum between the presence and absence of DPC. The most intense band at 1611 cm^{-1} and the weaker bands at 1208 and 1178 cm^{-1} derive mainly from the aromatic ring vibrations of the tyrosine residue. CH_2 bending from

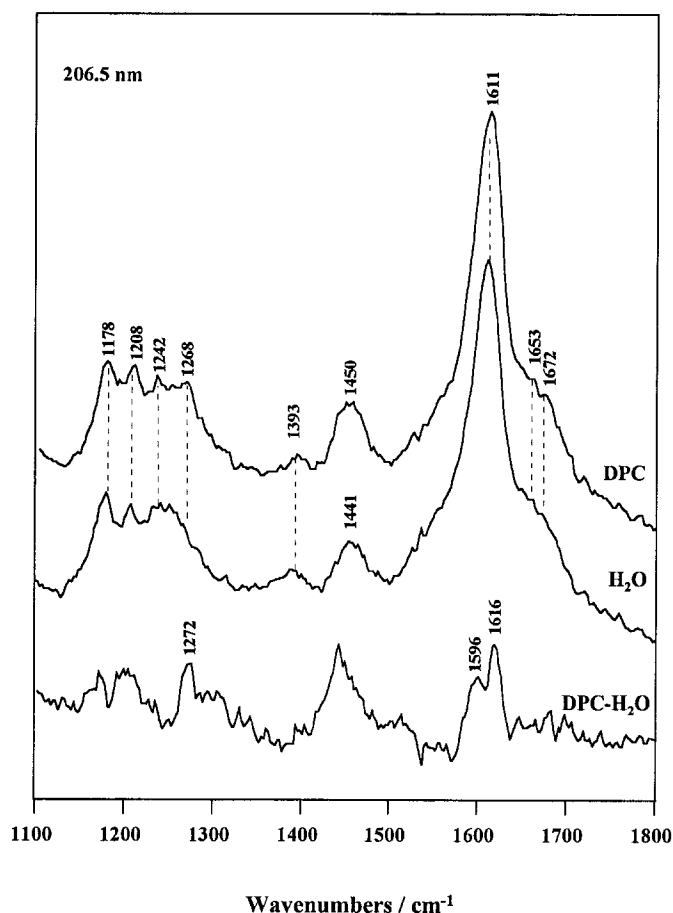


FIG. 7. The 206.5-nm excited Raman spectra of angiotensin II (AII) dissolved in H_2O , in dodecylphosphocholine (DPC), and the Raman difference spectrum of AII with and without DPC. Laser power was $\sim 3\text{ mW}$ with a spot size $\sim 150\text{ }\mu\text{m}$. The total accumulation time for all spectra is 33 min. The spectral resolution is $\sim 25\text{ cm}^{-1}$.

amino acid side-chain methylenes gives rise to the broad band centered $\sim 1450\text{ cm}^{-1}$ for AII in water.^{37,41} The more intense 1441-cm^{-1} band in the spectrum of AII in DPC derives from the overlap of methylene vibrations of the DPC with the amino acid side-chain methylenes.

The amide I vibrations give rise to shoulders^{40,41} at 1653 and 1672 cm^{-1} , while the weaker 1393-cm^{-1} band is due to the amide $\text{C}_\alpha\text{-H}$ bending vibration. The bands at 1242 and 1268 cm^{-1} mainly result from the amide III vibrations.^{40,41} The positions of the amide I bands at 1653 and 1672 cm^{-1} and amide III bands at 1242 and 1268 cm^{-1} suggest that AII in aqueous environments contains random coil, β -turn, and β -sheet conformations.^{40,41}

The AII conformational alterations between aqueous solution and the micelles is most easily monitored in the Fig. 7 difference spectrum. The amide III difference spectral peak at 1272 cm^{-1} suggests an increase in the β -turn content.⁴⁰ This result is helpful in defining the unique conformational structures that AII may adopt in hydrophobic environments, such as those found in the proximity of the receptor site. More information on AII conformation is reported elsewhere.⁵⁰

UV Raman and Photoluminescence Diamond Structural Studies. Diamond was one of the first materials studied by Raman spectroscopy;⁵¹ Raman measurements with visible wavelength excitation are now the standard monitor of diamond structure.⁵² Recently we demonstrated that near-bandgap (228.9 and 244 nm) excited Raman spectra of CVD diamond avoid the broad luminescence bands that interfere with measurements of the first- and second-order diamond phonon bands with the use of visible wavelength excitation.³⁶ For example, 228.9-nm UV Raman spectra of CVD and gem-quality diamond excited close to the $\sim 225\text{ nm}$ bandgap are shown in Fig. 8. The diamond spectrum can be separated into three regions based on the number of phonons involved in the scattering process. The first-order diamond phonon band (1332 cm^{-1}) results from the scattering of a single optical phonon at the maximum, in the diamond lattice-dispersion curve.⁵³ Two-phonon scattering in diamond produces a complex band with a maximum at 2467 cm^{-1} and a sharp cutoff at 2667 cm^{-1} . The second-order phonon bands of diamond are resonance enhanced with UV excitation; their intensity relative to the first-order phonon band increases tenfold in comparison to results from visible excitation.^{36,54} Three-phonon scattering in diamond produces a band with maxima at $\sim 3690\text{ cm}^{-1}$ in CVD diamond.³⁶ The bands observed in the 228.9-nm excited third-order phonon region of the gem-quality diamond are probably not Raman bands, but rather photoluminescence (PL) bands associated with the N9 defect center (Fig. 8C).⁵³⁻⁵⁸

On the basis of 228.9-nm excited Raman spectra of different CVD diamond samples, the intensity ratio of the diamond third-order phonon band to the second-order phonon band appears to be sensitive to either the diamond crystallite size or the crystallite orientation. Photoluminescence, while sensitive to the crystallite size, appears to be most sensitive to impurities within the diamond crystallites (*vide infra*).

The Raman spectrum of CVD diamond excited at 206.5 nm , deep within the electronic bandgap, is shown in Fig. 9. The 206.5-nm excited Raman spectrum is sim-

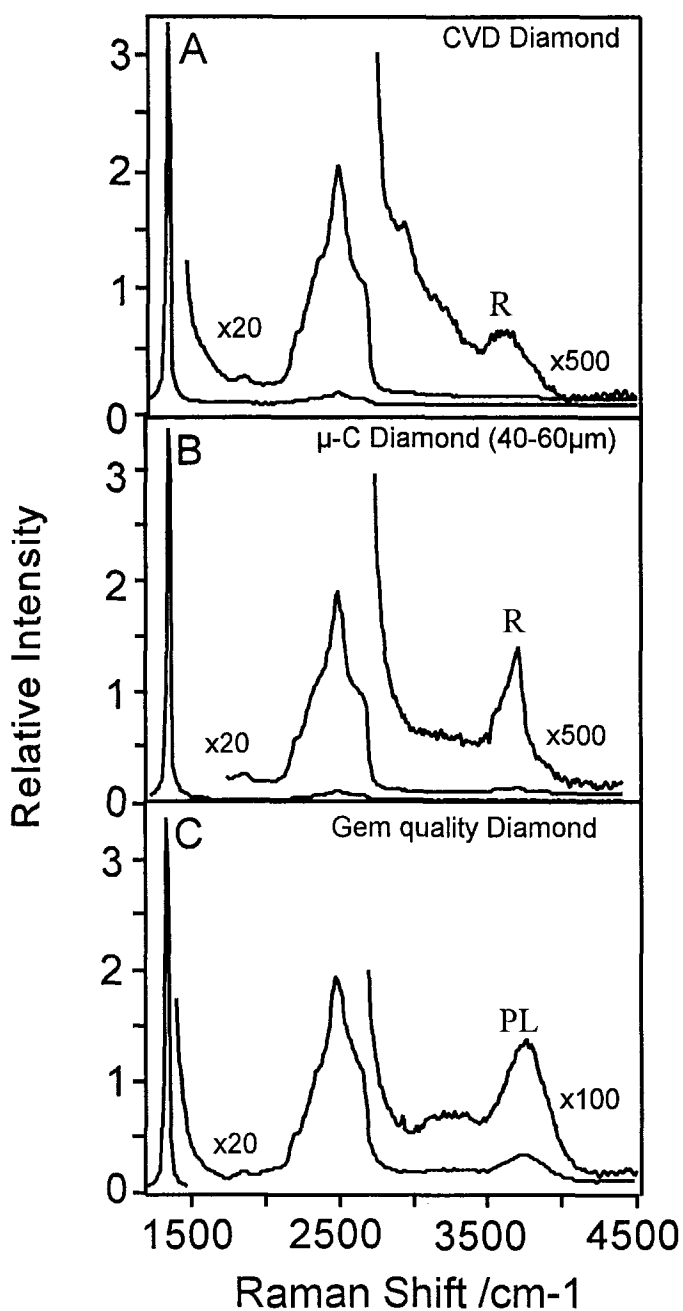


FIG. 8. The 228.9-nm excited Raman spectrum of (A) optical-grade CVD diamond; (B) natural microcrystalline diamond powder ($40\text{--}60\text{ }\mu\text{m}$); (C) large gem-quality diamond. Laser spot size was $\sim 50\text{ }\mu\text{m}$ with an incident power of $\sim 7\text{--}10\text{ mW}$. Total-integration time used was $\sim 10\text{ s}$ for the first-order phonon band and 200 s for the second- and third-order phonon bands. The spectral resolution is 25 cm^{-1} . (R = Raman bands, and PL = photoluminescence bands.)

ilar to the spectrum excited at 228.9 nm (Fig. 8A), but the second-order phonon band intensity at $\sim 2200\text{ cm}^{-1}$ increases relative to that of the first-order phonon band. No broad-band luminescence appears between 206.5 and 225 nm with the 206.5-nm excitation directly within the diamond bandgap. The spectrum of the gem-quality diamond (Fig. 10) shows a series of narrow PL bands in the $225\text{--}260\text{-nm}$ spectral region, which were previously observed in cathodoluminescence studies.⁵⁹ The 206.5-nm excitation occurs well within the diamond elec-

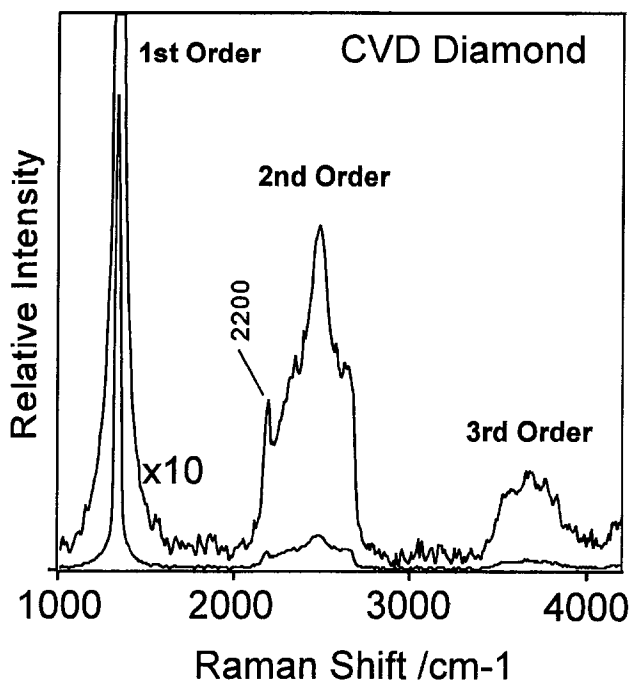


FIG. 9. The 206.5-nm excited Raman spectrum of CVD diamond. Laser power was ~ 3 mW with the same focusing conditions and spectral resolution as in Fig. 8. The detector was an ICCD array with a total integration time of 150 s for the first-order phonon band and 1000 s for the second- and third-order phonon bands.

tronic bandgap where the absorptivity is ~ 5000 cm^{-1} , and where penetration of 206.5-nm light is less than 1 μm into the crystal. Since the first-order phonon Raman scattered light also occurs within this bandgap, most of the Raman scattering and PL occur from a 500-nm-thick surface layer.

With 228.9-nm excitation of gem-quality diamond, we observe the expected first- and second-order Raman bands, as well as a band at ~ 3800 cm^{-1} , which we earlier assigned to the third-order phonon band.³⁶ However, this 3800- cm^{-1} band with 228.9-nm excitation occurs at 250.6 nm, which is identical in wavelength to the PL bands observed in the 206.5-nm excited spectrum of gem-quality diamond. Additionally, with 228.9-nm excitation, a smaller band occurs at ~ 3200 cm^{-1} , which corresponds to 247 nm. Since the peaks observed in the 228.9-nm Raman spectrum (Fig. 8C) match the frequencies and the intensity ratios of the peaks observed in the 206.5-nm photoluminescence spectrum (Fig. 10B), it is likely that the 3200- and 3800- cm^{-1} bands observed with 228.9-nm excitation are not Raman bands, but are PL bands which result from defect structures.

Figure 10A compares the 206.5-nm excited spectrum, between 225 and 260 nm, of CVD diamond to the spectrum of gem-quality diamond (Fig. 10B). The CVD diamond shows strong resolvable peak maxima at ~ 230 , 235, and 242 nm, and a broad complex band at wavelengths longer than 260 nm. The gem-quality diamond spectrum also shows a weak band at 230 nm, and strong PL bands with maxima at ~ 236 , 240, 243, 247, and 251 nm, which are narrower than those of the CVD diamond. The above bands, which are also observed by cathodoluminescence, result from the recombination of free and defect-bound electron hole pairs (excitons).⁵³ These band-

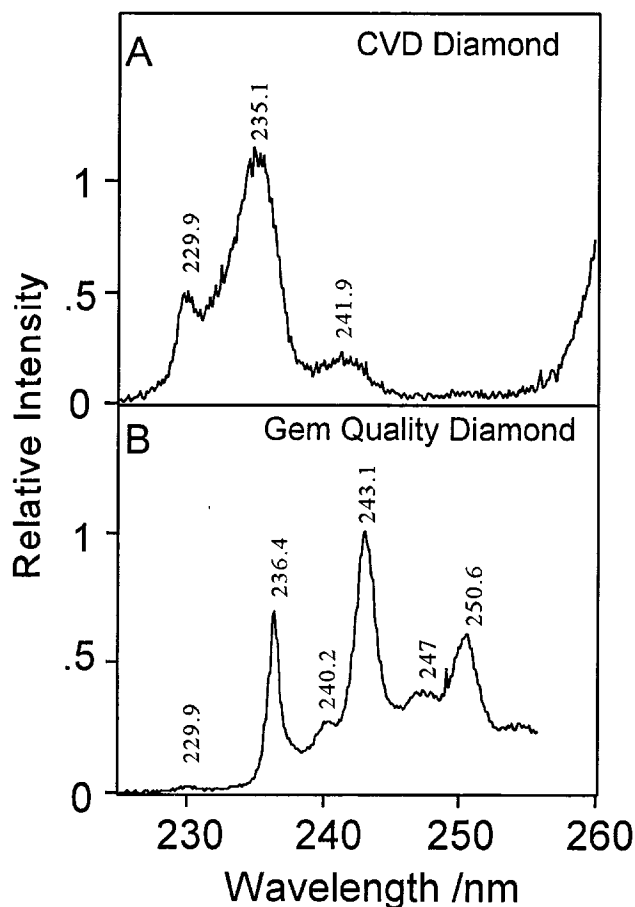


FIG. 10. The 206.5-nm excited emission spectrum of (A) CVD film and (B) gem-quality natural diamond. The CVD spectrum was collected with a total integration time of 150 s by an ICCD. The natural diamond emission spectrum was collected by an ICCD with a total integration time of 100 s at ~ 50 cm^{-1} spectral resolution.

widths increase with temperature, and the intensities decrease as the crystal perfection decreases.⁵³⁻⁵⁸

The 230-nm emission band is the only band with an identical frequency for the CVD diamond films and the gem-quality diamond. The energy of the 230-nm band coincides both with the expected energy of the fourth-order Raman phonon band of diamond at 4950 cm^{-1} (2×2470 cm^{-1}) and with the indirect exciton energy gap.^{55,57,58} If we shift the excitation wavelength from 206.5 to 210 nm for the CVD diamond, the 230-nm band is not observed in the emission spectrum (Fig. 11A, solid line). The difference spectrum between the 206.5- and 210-nm excited PL spectra (Fig. 11B) does not show the positive and negative bands that would be expected if the 230-nm band simply shifted to overlap the stronger 234-nm PL band. However, the presence of the two positive peaks in the PL difference spectrum may be an artifact associated with the use of the 210-nm, high-peak-power, pulsed laser excitation source. Although the 206.5- and 210-nm PL spectra were measured with approximately the same average power, the high pulse peak power of the 210-nm excitation (15 ns pulses, 200 Hz) may preferentially probe those excitons with short lifetimes, since the long-lived excitons saturate during the short pulse duration. A similar saturation effect has also been observed for the cathodoluminescence measure-

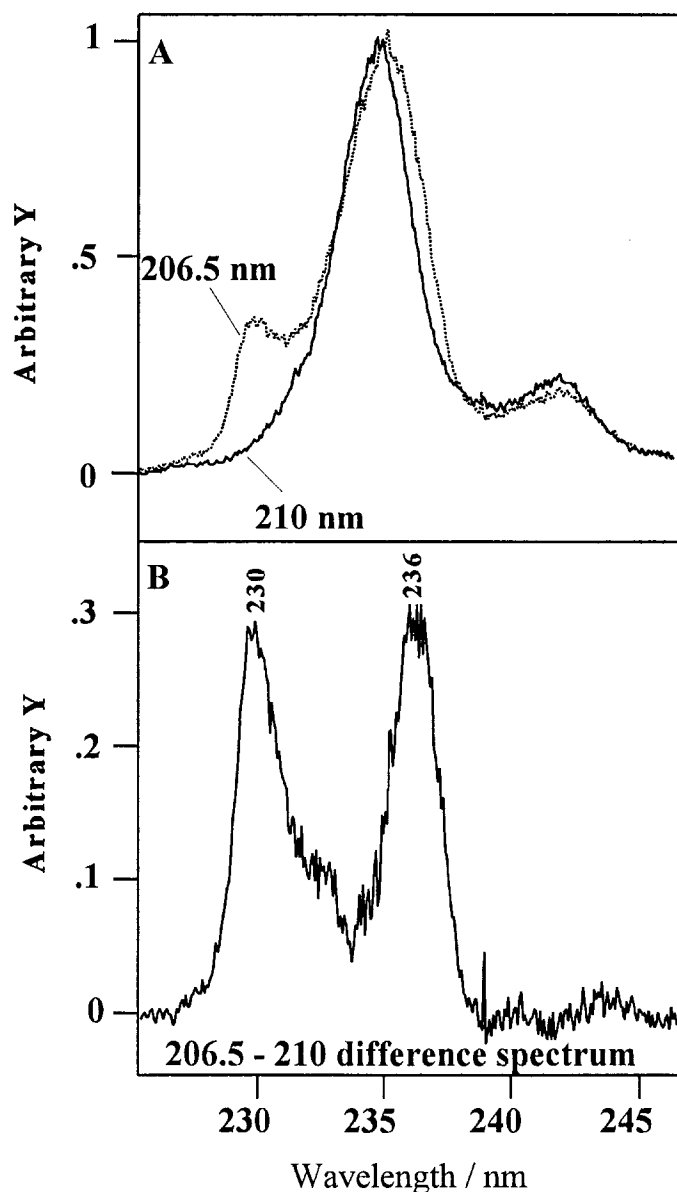


FIG. 11. The 210-nm (solid line) and 206.5-nm (dashed line; Fig. 9) excited emission spectrum of CVD diamond. The 210-nm excited spectrum was obtained with a frequency-doubled 200-Hz excimer laser pumped dye laser with an average power of 1.5 mW, focused to a ~ 50 - μm spot size. The data were detected by an intensified Reticon diode array with a total integration time of 150 s at ~ 50 cm^{-1} spectral resolution.

ments of the diamond A band luminescence as the electron energy or current is increased.⁵⁹ Therefore, we cannot as yet unambiguously assign the 230-nm band either as the diamond fourth-order phonon band or as a result of direct free exciton recombinations.

The 206.5-nm excitation of the CVD diamond allows us to evaluate the quality and defect density of diamond films. The Raman first-order phonon band and the edge-emission bands region are both sensitive to the defect density and nondiamond impurities present in the films. Furthermore, the bandgap emission (230 to 255 nm), previously studied only by cathodoluminescence, can now be monitored with the 206.5-nm excitation. We are now studying the relationship between the concentrations, and

types of nondiamond carbon impurities, and the resulting near-bandgap photoluminescence and Raman band intensities and frequencies.

CONCLUSION

We have demonstrated the utility of a new 206.5-nm continuous-wave excitation source for UV Raman spectral measurements of protein secondary structure and for studies of diamond. The 206.5-nm Raman spectra can be conveniently used to monitor protein and peptide secondary structure in aqueous solution and lipid micelles. We have also demonstrated that 206.5-nm excitation, which occurs within the diamond bandgap, can be used to excite photoluminescence from diamond defects. This approach is an additional powerful methodology for studying diamond defect structures. Some of the spectral features are similar to those observed by cathodoluminescence, but the 206.5-nm excitation measurements are simple and do not require high vacuum.

ACKNOWLEDGMENTS

We gratefully acknowledge support from NIH Grant R01GM30741-13 (to S.A.A.). This work was also supported by the AFOSR grant to the University of Pittsburgh Materials Research Center (F49620-95-1-0167).

1. M. B. Robin, in *Higher Excited States of Polyatomic Molecules* (Academic Press, Orlando, Florida, 1979), Vols. I and II.
2. J. M. Dudik, C. R. Johnson, and S. A. Asher, *J. Chem. Phys.* **82**, 1732 (1985).
3. J. M. Dudik, C. R. Johnson, and S. A. Asher, *J. Phys. Chem.* **89**, 3805 (1985).
4. D. A. Long, in *Raman Spectroscopy* (McGraw-Hill, New York, 1977).
5. S. A. Asher, *Ann. Rev. Phys. Chem.* **39**, 537 (1988).
6. A. B. Myers and R. A. Mathies, in *Biological Applications of Raman Spectroscopy*, T. G. Spiro, Ed. (John Wiley and Sons, 1987), Vol. 2, pp. 1-58.
7. S. A. Asher and C. R. Johnson, *Science* **225**, 311 (1984).
8. S. A. Asher, C. R. Johnson, and J. Murtaugh, *Rev. Sci. Instrum.* **54**, 1657 (1983).
9. S. A. Asher, *Anal. Chem.* **65**, 59 A (1993); S. A. Asher, *Anal. Chem.* **65**, 201 A (1993).
10. C. R. Johnson, M. Ludwig, S. O'Donnell, and S. A. Asher, *J. Am. Chem. Soc.* **106**, 5008 (1984).
11. T. G. Spiro, G. Smulevich, and C. Su, *Biochemistry* **29**, 4497 (1990).
12. I. Harada, T. Yamagishi, K. Uchida, and H. Takeuchi, *J. Am. Chem. Soc.* **112**, 2443 (1990).
13. R. A. Copeland and T. G. Spiro, *Biochemistry* **26**, 2134 (1987).
14. J. A. Sweeney, P. A. Harmon, S. A. Asher, M. Hutnik, and A. G. Szabo, *J. Am. Chem. Soc.* **113**, 7531 (1991).
15. N. Cho, S. Song, and S. A. Asher, *Biochemistry* **33**, 5932 (1994).
16. S. A. Asher, P. J. Larkin, and J. Teraoka, *Biochemistry* **30**, 5944 (1991).
17. N. Cho and S. A. Asher, *J. Am. Chem. Soc.* **115**, 6349 (1993).
18. S. P. A. Fodor and T. G. Spiro, *J. Am. Chem. Soc.* **108**, 3198 (1986).
19. W. L. Kubasek, B. Hudson, and W. Peticolas, *Proc. Natl. Acad. Sci. USA* **82**, 2369 (1985).
20. R. G. Efremov, A. V. Feofanov, K. N. Dzhandzhugazyan, N. N. Modyanov, and I. R. Nabiev, *FEBS Lett.* **260**, 257 (1990).
21. S. A. Asher, *Anal. Chem.* **56**, 720 (1984).
22. C. M. Jones, T. A. Naim, M. Ludwig, J. Murtaugh, P. F. Flaugh, J. M. Dudik, C. R. Johnson, and S. A. Asher, *Trends Anal. Chem.* **4**, 75 (1985).
23. R. Rummelfanger, S. A. Asher, and M. B. Perry, *Appl. Spectrosc.* **42**, 267 (1988).
24. C. M. Jones and S. A. Asher, *J. Chem. Phys.* **89**, 2649 (1988).
25. C. M. Jones, V. L. Devito, P. A. Harmon, and S. A. Asher, *Appl. Spectrosc.* **41**, 1268 (1987).

26. J. Teraoka, P. A. Harmon, and S. A. Asher, *J. Am. Chem. Soc.* **112**, 2892 (1990).
27. P. A. Harmon, J. Teraoka, and S. A. Asher, *J. Am. Chem. Soc.* **112**, 8789 (1990).
28. M. Ludwig and S. A. Asher, *J. Am. Chem. Soc.* **110**, 1005 (1988).
29. S. A. Asher, R. W. Bormett, X. G. Chen, D. H. Lemmon, N. Cho, P. Peterson, M. Arrigoni, L. Spinelli, and J. Cannon, *Appl. Spectrosc.* **47**, 628 (1993).
30. X. G. Chen, R. Schweitzer-Stenner, S. A. Asher, N. G. Mirkin, and S. Krimm, *J. Phys. Chem.* **99**, 3074 (1995).
31. X. G. Chen, S. A. Asher, R. Schweitzer-Stenner, N. G. Mirkin, and S. Krimm, *J. Am. Chem. Soc.* **117**, 2884 (1995).
32. L. C. Mayne, L. D. Ziegler, and B. Hudson, *J. Phys. Chem.* **89**, 3395 (1985).
33. L. C. Mayne and B. Hudson, *J. Phys. Chem.* **95**, 2962 (1991).
34. Y. Wang, R. Purrello, T. Jordan, and T. G. Spiro, *J. Am. Chem. Soc.* **113**, 6359 (1991).
35. Y. Wang, R. Purrello, S. Georgiou, and T. G. Spiro, *J. Am. Chem. Soc.* **113**, 6368 (1991).
36. R. W. Bormett, S. A. Asher, R. E. Witkowski, W. D. Partlow, R. Lizewski, and F. Pettit, *J. Appl. Phys.* **77**, 5916 (1995).
37. S. Song and S. A. Asher, *J. Am. Chem. Soc.* **111**, 4295 (1989).
38. S. A. Asher, M. Ludwig, and C. R. Johnson, *J. Am. Chem. Soc.* **108**, 3186 (1986).
39. R. Rava and T. G. Spiro, *J. Phys. Chem.* **89**, 1856 (1985).
40. A. T. Tu, in *Spectroscopy of Biological Systems*, R. J. H. Clark and R. E. Hester, Eds. (John Wiley and Sons, New York, 1986), Vol. 13, pp. 47–112.
41. I. Harada and H. Takeuchi, in *Spectroscopy of Biological Systems*, R. J. H. Clark and R. E. Hester, Eds. (John Wiley and Sons, New York, 1986), Vol. 13, pp. 113–175.
42. R. A. Copeland and T. G. Spiro, *J. Am. Chem. Soc.* **108**, 1281 (1986).
43. M. Ludwig and S. A. Asher, *J. Am. Chem. Soc.* **110**, 1005 (1988).
44. Z. Chi, X. G. Chen, J. S. W. Holtz, and S. A. Asher, paper submitted to *Biochemistry*.
45. D. M. Byler and H. Susi, *Biopolymers* **25**, 469 (1986).
46. P. Pancoska, S. C. Yasui, and T. A. Keiderling, *Biochemistry* **30**, 5089 (1991).
47. J. T. Yang, C. S. C. Wu, and H. M. Martinez, *Methods Enzymol.* **130**, 208 (1986).
48. N. Kossovsky, A. Nguyen, K. Sukiassians, A. Festekjian, A. Gelman, and E. Sponsler, *J. Colloid Interface Sci.* **166**, 350 (1994).
49. I. Reid, B. Morris, and W. Gannog, *Ann. Rev. Physiol.* **40**, 377 (1978).
50. N. Cho and S. A. Asher, *Biospectroscopy* **2**, 71 (1996).
51. D. S. Knight and W. B. White, *J. Mater. Res.* **4**, 385 (1989).
52. S. A. Solin and A. K. Ramdas, *Phys. Rev.* **1**, 1687 (1970).
53. P. J. Dean, E. C. Lightowers, and D. R. Wight, *Phys. Rev.* **140**, A352 (1965).
54. J. M. Calleja, J. Kuhl, and M. Cardona, *Phys. Rev. B* **17**, 876 (1978).
55. D. R. Wight and P. J. Dean, *Phys. Rev.* **154**, 689 (1967).
56. P. J. Dean and I. H. Jones, *Phys. Rev. A* **133**, 1698 (1964).
57. L. H. Robins, E. N. Farabaugh, and A. Feldman, *Phys. Rev.* **48**, 14167 (1993).
58. H. Guo and M. Alam, in *Applications of Diamond Related Materials*, Y. Tzeng, M. Yoshikawa, M. Murakawa, and A. Feldman, Eds. (Elsevier Science Publishers B.C., Amsterdam, 1991).
59. P. J. Dean, *Phys. Rev.* **139**, A588 (1965).